Ionics
https://doi.org/10.1007/s11581-024-05729-5

RESEARCH

Biogenic synthesis of $LiNiVO_4$ nanoparticles for the evaluation of photocatalytic and electrochemical applications

M. Thejaswini[1] · V. Lakshmi Ranganatha[2] · C. Mallikarjunaswamy[1] · S. Pramila[1] · G. Nagaraju[3]

Received: 7 March 2024 / Revised: 17 July 2024 / Accepted: 18 July 2024

Abstract

In this present work, lithium nickel vanadate nanoparticles ($LiNiVO_4$ NPs) were synthesized by solution combustion method. Here, jackfruit seed extract is employed as a fuel for the synthesis. These nanoparticles were characterized by various spectroscopic techniques. X-ray diffraction (XRD) studies confirm the inverse spinel structure of $LiNiVO_4$ NPs. The scanning electron microscopy (SEM) images represent the agglomerated and clustered-like structure of NPs. Energy dispersive X-ray (EDX) spectrometry shows the existence of vanadium, nickel, and oxygen elements. Also, Ni and V are present in the average ratio of 1:1. The UV–visible spectral analysis indicated absorption bands at 465 and 728 nm, corresponding to a band gap energy of 2.2 eV. The vibrational analysis of the NPs was confirmed through IR and Raman spectroscopy, with a new peak observed at 1036 cm^{-1} indicating the bond interaction of Li^+-O-V in the FTIR analysis. Further, $LiNiVO_4$ NPs exhibit good photocatalytic activity for the degradation of methylene blue (MB) dye under visible light irradiation. And the percentage of degradation efficiency is 91.77 around 180 min. The photocatalytic activity was due to the production of OH radicals during photo irradiation on $LiNiVO_4$ NPs. The effect of different parameters on photo-catalytic activity was also studied in detail, including dye concentration, catalytic quantity, pH variation, scavenger activity, and recycling of the catalyst. Electrochemical impedance spectroscopy analysis revealed lower charge transfer and good ionic conductivity of LNV NPs, and it is also suitable for supercapacitor preparation.

Keywords Solution combustion · Photocatalytic · Electrochemical · Impedance

Introduction

The word nano means dwarf is derived from the Greek word nanos [1]. Nanoparticles are defined as particles between 1 and 100 nanometers in size. Nanoscience and nanotechnology are the analysis of very small particles and have many applications in engineering, chemistry, physics, biology, and material science. Nanostructure science is a broad and multidisciplinary field of research and development, which has been growing exponentially worldwide in recent years. Nanoparticles have several applications in the fields of healthcare, electronics, agriculture, automobiles, optical, magnetic transport, photochemical, electrochemical, catalytic, and mechanical behavior [2].

Lithium-containing transition metal vanadium oxide nanoparticles have wide applications in the field of rechargeable batteries due to their high cell voltage and spinal or inverse spinal structure [3]; there are $LiNiVO_4$ [4, 9–11], $LiMnVO_4$ [5], $LiCoVO_4$ [6], $LiNiCoVO_4$[7], and $LiNiMnVO_4$[8]. Here, Li and transition metal occupy the octahedral site. V atom occupies the tetrahedral site, and the 32e site by O ions [12]. In the latter years, $LiNiVO_4$ nanomaterials have been largely used as high-voltage lithium cell materials for many applications in electric vehicles, plug-in hybrid electric vehicles, removal of low energy density cells, health hazards, and small cell applications.

✉ C. Mallikarjunaswamy
mallik.aanekere@gmail.com

[1] Postgraduate Department of Chemistry, JSS College of Arts, Commerce, and Science and JSS Research Centre (A Recognized Research Center of the University of Mysore), Mysuru 570025, Karnataka, India

[2] Department of Chemistry, The National Institute of Engineering, Manandavadi Road, Mysuru 570008, Karnataka, India

[3] Energy Materials Research Laboratory, Department of Chemistry, Siddaganga Institute of Technology, Tumakuru 572103, Karnataka, India

Published online: 25 July 2024

The group VA transition metal oxides exhibit efficient photocatalytic activities under visible light irradiation [12]. A massive scientific investigation has been carried out on the preparation, characterization, and photodegradation studies of VA transition metal oxides, such as V_2O_5 [13], $LaVO_4$ [14, 15], $BiVO_4$ [16], $Sn_2Nb_2O_7$ [17], Ag_3VO_4 [18, 19], ZrV_2O_7 [20], $LiNiVO_4$ [12], $CaZnV_2O_7$ [21], $NiVO_3$ [22], $Ni_3V_2O_8$ [23], Ni_2FeVO_6 [24], and $Ni_3V_2O_8$ [25]. Among this inverse spinal structure of $LiNiVO_4$ NPs shows superior photodegradation activity under visible light illumination. Here, Li^+ and Ni^{2+} ions were distributed in octahedral sites. V^{5+} ion residue was distributed in the tetrahedral site. In the $LiNiVO_4$ lattice, multi-valence electrons of Ni and V ions might be present. The deintercalation process of Li^+ ions leads to the oxidation of Ni^{II} into Ni^{III} oxidation states, and it is due to the non-oxidative of V atoms. When $LiNiVO_4$ is exposed to visible light, electrons are produced by photoreceptors. Then, electrons are transferred from oxygen 2p orbitals to the empty 3d Ni orbitals or by transfer of electrons from O 2p to the empty 3d V^{5+} orbital [12]. Therefore, H^+ (holes) and free electrons are generated on the surface of the photocatalyst. These convert toxic organic dye into a nontoxic degradable product. The photodegradable properties mainly depend on grain size, synthetic method, and sintering temperature.

Many methods have been used to synthesize $LiNiVO_4$ nanoparticles such as hydrothermal [26], solid state [10], sol–gel [7, 11], and Pechini method [12]. In this paper, lithium nickel vanadate nanoparticles are first time prepared by combustion method. It is a simple, inexpensive, easy, high yield, and energy-saving method. In nanoparticle synthesis, chemicals like polyvinyl alcohol, ascorbic acid, and sodium citrate are used as reducing and capping agents. These chemicals are always toxicant to nature which leads to pollution in the environment. However, to overcome this problem, plant biomass/juice such as *Aloe barbadensis* [27], *Carica papaya* [28], *Corymbia citriodora* [29], *Eucalyptus globules* [30], and *Lycopersicon esculentum* [31] has been used as a fuel. They act as a capping and reducing agent and are low-price, nontoxic, and environment friendly.

In this study, $LiNiVO_4$ NPs use the green synthesis followed by the solution combustion method. Here, jackfruit seed extract was employed as taken initially for the green synthesis reaction. Jackfruit (*Artocarpus heterophyllus*) [32] belongs to the Moraceae family, which has antioxidant, anti-inflammatory, antifungal, hypoglycemic, and wound-healing properties. It also played a very important role in the reduction of metal ions into nanoparticles due to their bioactive substances like flavonoids and alkaloids in the extract. Within the framework of these criteria, XRD, SEM, EDS, FTIR, Raman, and UV–vis analysis were applied to characterize the properties of synthesized products. Additionally, textile industries' waste organic product like methylene blue was used to analyze efficient photocatalytic activities of $LiNiVO_4$ NPs under visible light irradiation and also tested the electrochemical impedance spectroscopy.

Experimental section

Materials and methods

Lithium carbonate (Li_2CO_3, 99%), nickel nitrate ($Ni(NO_3)_2$, 99%), ammonium vanadate (NH_4VO_3, 99%), potassium chloride (KCl, 99.9%), and methylene blue (MB, 97%) was purchased from SD Fine Chemicals. All the chemicals used were analytical grade and used without further purification.

Preparation of jackfruit extract

Fresh and unripe jackfruit was procured from IIHR, Bangalore. The jackfruits were meticulously washed, cut into small pieces, and subsequently dried. These dried pieces were then blended to produce jackfruit flour. The obtained flour was transferred to a Soxhlet extractor, and extraction was conducted using distilled water as a solvent.The resulting extract was collected and stored in the refrigerator for subsequent experiments.

Preparation of *lithium* nickel vanadate nanoparticles

Lithium nickel vanadate was synthesized by a simple combustion method. For the synthesis of $LiNiVO_4$ nanoparticles, tender jackfruit seed extract was taken as fuel. A stoichiometric amount of lithium carbonate (Li_2CO_3), nickel nitrate ($Ni(NO_3)_2$), and ammonium vanadate (NH_4VO_3) was taken in a silica crucible. To this, different volume of fuel was added (2 ml, 4 ml, 6 ml, and 8 ml) and labeled as LNV1, LNV2, LNV3, and LNV4, respectively. Further, this mixture was placed on a hot plate with continuous stirring to get a homogeneous mixture. Then, this series of $LiNiVO_4$ was subjected to preheated muffle furnace at 400 °C for about 10 min separately. Calcination was carried out to remove impurities from the synthesized product at 500 °C for 5 h. Finally, pure, olive-green color lithium nickel vanadate was obtained and used for further analysis.

Characterization

The crystallinity and purity of the synthesized LNV NPs were identified using an XRD in the Rigaku smart lab (cu-kα). The elemental analysis, particle size, and morphology of the nanoparticles were elucidated by TESCN Vega 3LMO SEM. UV–vis spectrophotometer was used to analyze the optical properties of the NPs (Agilent Cary

60). The functional groups of the nanoparticles were recognized using an FTIR spectrophotometer (FTIR-Bruker Alpha). The range of wave numbers is between 400 and 1200 cm^{-1}. The Raman measurement of synthesized nanoparticles was recorded by using Horiba Xplora plus Raman spectroscope.

Photodegradation study of nanoparticles

Lithium nickel vanadate nanomaterials were synthesized by the combustion method. The photo-degradation efficiency of $LiNiVO_4$ NPs was evaluated by using methylene blue dye under visible light radiation using a 300 W/230 V AC tungsten lamp at room temperature. The different parameter effects of photodegradation such as different concentrations of catalyst load, variable dye concentration, pH variation, and scavenger activity have been studied using $LiNiVO_4$ nanoparticles. In this method, a known amount of photocatalyst (10–70 mg) was mixed with 100 ml of MB solution (5 ppm). Further, this mixture was added under a dark chamber with continuous stirring for about 30 min to observe adsorption/desorption between photocatalyst and methylene blue organic dye. After that, around 2 ml of the mixture was withdrawn from the photoreactor, followed by a centrifugation to remove the catalyst. The sample was subjected to visible light at wavelength 664 nm. The percentage of degradation was calculated using the following formula.

$$\text{Degradation percentage} = \frac{C_0 - C_f}{C_0} \times 100 \quad (1)$$

where C_0 is the initial absorbance and C_f is the final absorbance of every 30 min.

Modified electrode preparation for electrochemical study

5 mM KCl and three-electrode cyclic voltammetry were used to analyze the EIS of lithium nickel vanadate nanoparticles. 4 mg of the sample was dissolved in deionized water and sonicated for up to 10 min. The impurities on the surface of the glassy carbon electrode were removed by polishing using MRE paper (1.0, 0.3, and 0.05 different grain sizes) for 3 min. The surface of the electrode was coated by a drop casting technique and dried for 4 h. For the analysis of EIS, glassy carbon, platinum, and silver-silver electrodes were used as a three-electrode system.

Result and discussion

X-ray diffraction studies

XRD pattern of lithium nickel vanadate nanoparticles prepared by combustion method was represented in Fig. 1. It clearly shows the inverse spinel structure of $LiNiVO_4$ nanoparticles [11]. Here, octahedral sites were occupied by Li and Ni atoms, vanadium ions were occupied on the tetrahedral sites (8a), and O atoms were on the 32e site [33]. The most intense line (220) indicates the transition metal atom present in the tetrahedral site. All four XRD patterns exhibit diffraction-dominated peaks at 2 θ = 36.28° and 30.84° related to the crystal planes of (220) and (311), respectively. This shows the strong crystalline nature of the nanoparticles [34]. The peaks labeled as * and # indicate the minute quantity of Li_3VO_4 and NiO impurities in the $LiNiVO_4$ NPs, respectively (according to several earlier researchers) [9, 34–38]. Using Debye Scherer's formula, the crystalline size of the $LiNiVO_4$ nanoparticles was calculated. The average crystalline size of the lithium nickel vanadate nanoparticle is 55 nm.

$$D = \frac{0.94\lambda}{\beta COS\theta} \quad (2)$$

Here, D is the average size of the crystal, λ is the wavelength of the X-ray source, θ indicates Braggs diffracting angle, and β is the full width at half maximum.

The lattice strain (ε) is an interesting structural parameter of LNV NPs and is calculated using the following equation

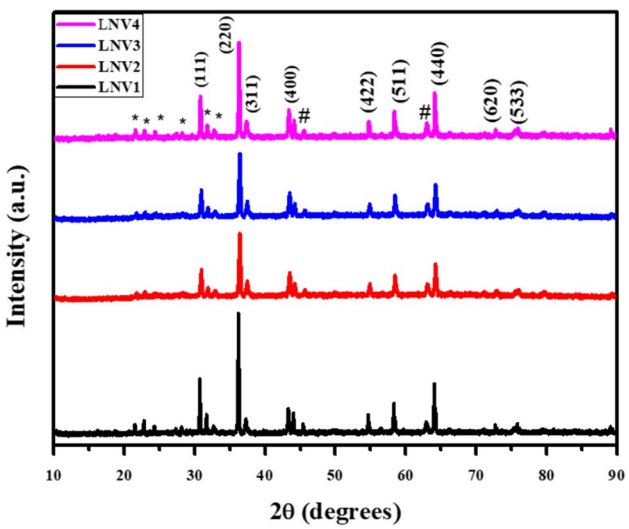

Fig. 1 XRD analysis of $LiNiVO_4$ NPs fabricated by combustion method (* -Li_3VO_4, #—NiO)

$$\varepsilon = \frac{\beta}{4\tan(\theta)} \tag{3}$$

The dislocation density of the LNV NPs was calculated using the below expression

$$\delta = \frac{1}{D^2} \tag{4}$$

The stacking fault energy of LNV NPs was calculated using the following equation.

$$2\pi^2/45(3\tan\theta)^{1/2} \tag{5}$$

The lattice constant was calculated using the following equation and is tabulated in Table 1.

$$\alpha = d_{hkl}\sqrt{h^2 + k^2 + l^2} \tag{6}$$

where h, k, and l are the Miller indices, and d is the interplane spacing of the crystal plane. It was observed that with increasing the fuel concentration, the lattice constant also increases from 6.141 to 6.203 Å. The calculated lattice strain and dislocation density are given in Table 1. It clearly explains that as the crystallite size increases, lattice strain and dislocation density decrease due to lattice imperfection. The stacking fault energy of LNV1 NPs is greater compared to LNV4 NPs due to their particle close together (Fig. 2).

Morphology study of nanoparticles

Figure 3 illustrates the SEM images of $LiNiVO_4$ nanoparticles synthesized by the combustion method using different concentrations of jackfruit seed extract as fuel. The images indicate the formation of agglomerated and clustered with almost spherical and needle structure morphology. During the synthesis, high energy generated from the muffle furnace even leads to the agglomeration of nanoparticles. The size of the nanoparticles decreases as the concentration of the fuel increases. Particle is in the range from 74 to 88 nm and also agglomeration increases with an increase in fuel concentration [9, 35]. Figure 3 (e) shows the energy dispersive

Table 1 Crystallographic data of LNV NPs

Sl no	Samples	2ɵ (°)	FWHM (radians)	Crystallite size (nm)	Lattice strain (nm)	Dislocation density (δ)	Staking fault (mJ/m^2)	d (Å)	a (Å)
1	LNV1	41.56	0.14	60.66	1.6098	0.2716	0.7103	2.1712	6.141
2	LNV2	41.52	0.15	56.76	1.6908	0.3102	0.6818	2.1732	6.146
3	LNV3	41.57	0.156	54.06	1.9026	0.3421	0.7174	2.1747	6.15
4	LNV4	41.12	0.167	50.78	1.9427	0.3877	0.4064	2.1934	6.2038

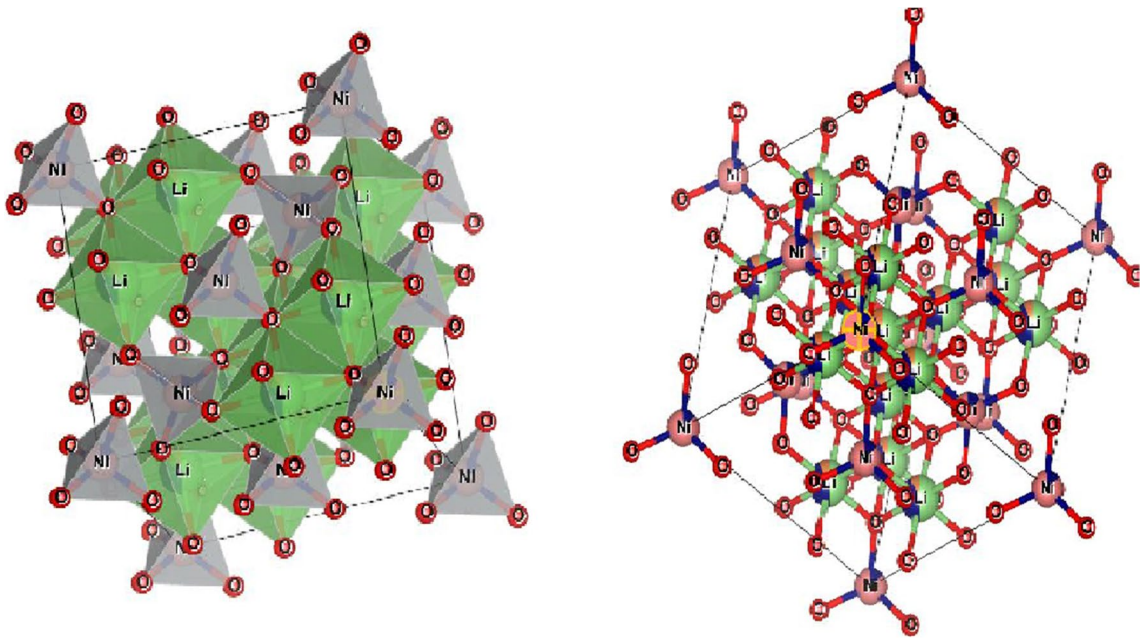

Fig. 2 Crystalline structure of LNV nanoparticles synthesized by combustion method

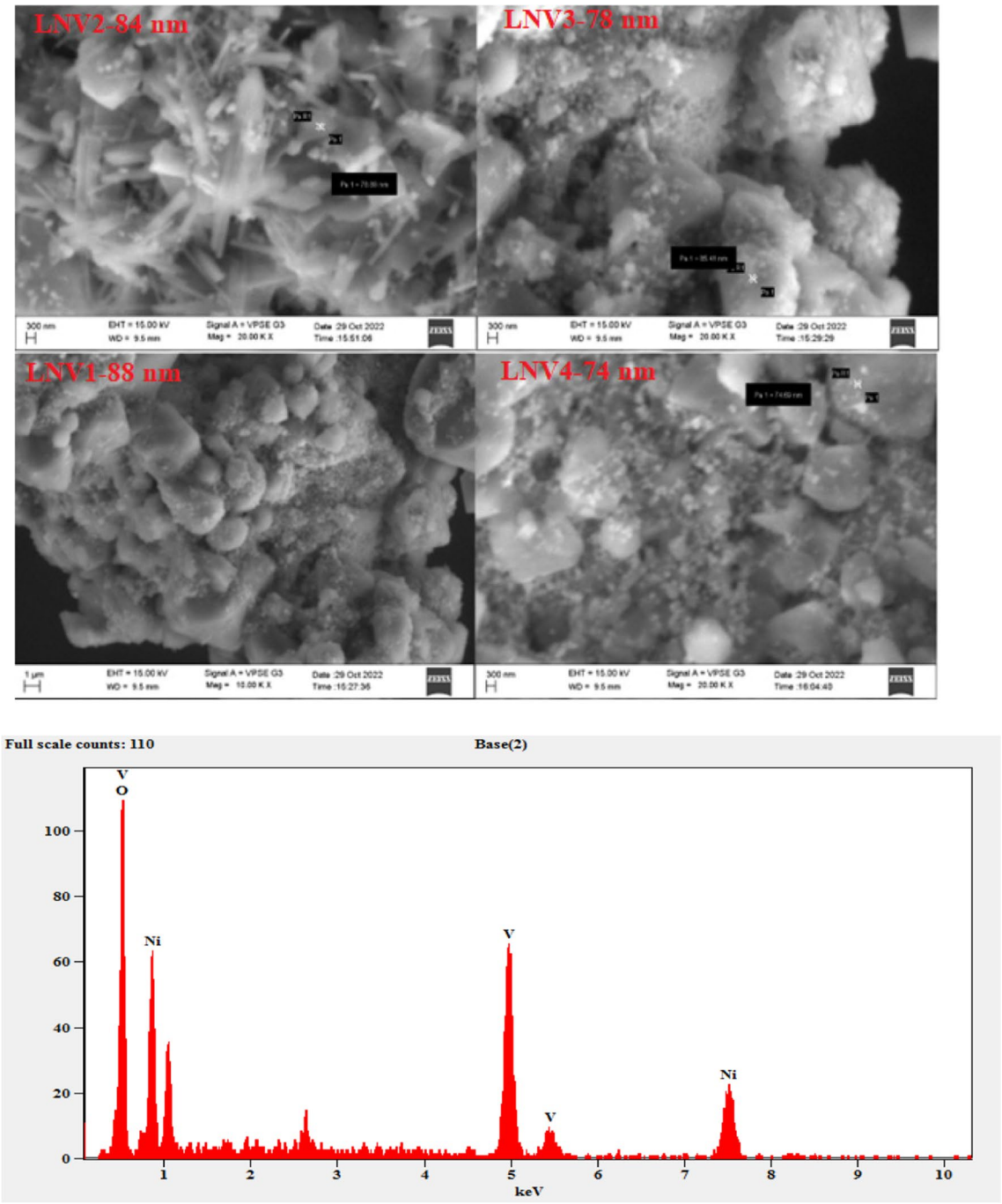

Fig. 3 SEM and EDS images of LNV4 nanoparticles synthesized using the combustion method

X-ray spectrometry (EDS). This represented the elemental composition of synthesized lithium nickel vanadate NPs. The analysis of EDS shows the existence of V, Ni, and oxygen elements (Table 2). Also, the presence of Ni: V in the average ratio is 1:1. however, the Li element cannot be detected because of the lightest metallic element [12] [39].

Table 2 Chemical composition of $LiNiVO_4$ NPs

Elements	Weight%	Atomic %	Error %
O K	52.28	78.95	1.93
V K	22.47	10.66	1.14
Ni K	25.25	10.39	2.64

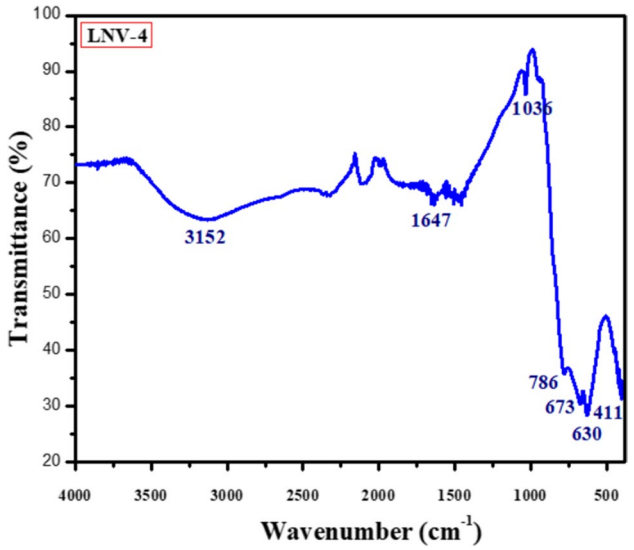

Fig. 4 FTIR spectral studies of $LiNiVO_4$ nanoparticles

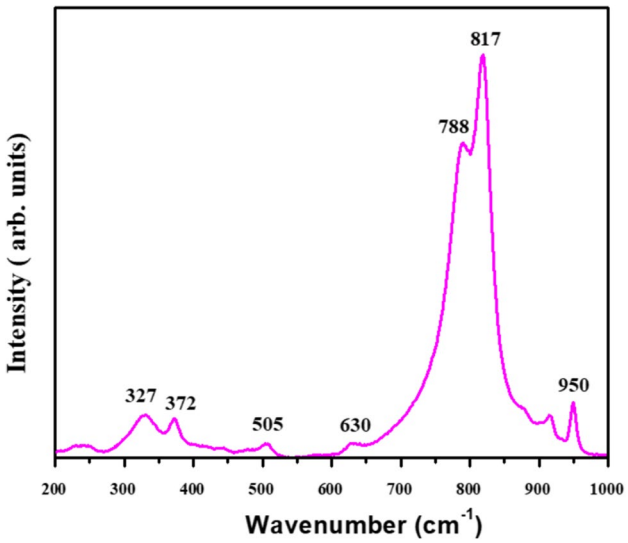

Fig. 5 Raman spectral analysis of $LiNiVO_4$ nanoparticles

Analysis of Fourier transforms infrared technique

Figure 4 represents FTIR spectra of $LiNiVO_4$ nanoparticles in the 400–4000 cm^{-1} range. Different bands located at 630, 673 and 786 cm^{-1} have been specified to VO_4 tetrahedrons stretching vibrations and also inverse spinel structure of characteristic vibrational bands. The asymmetrical stretching of Li-O in LiO_6 octahedrons was observed at 411 cm^{-1} region. There is a small peak around 1036 cm^{-1} which indicates Li^+-O-V band interactions. FTIR spectrum produces all the possible vibrational bands of $LiNiVO_4$ [10]. The peak at 1647 cm^{-1} is attributed to the bending H-O-H vibrational band. It is confirmed that some of the water molecules are attached to the LNV NPs. The peak that appeared in the higher frequency region at 3152 cm^{-1} represents the hydroxyl group stretching vibration of tetravalent vanadium [33, 34, 36].

Raman spectroscopy analysis

The vibrational property of the synthesized $LiNiVO_4$ nanoparticles was represented in Fig. 5 by using Raman spectroscopy. The different peaks of $LiNiVO_4$ are located at 327 cm^{-1}, 817 cm^{-1}, and 950 cm^{-1} corresponding to A_{1g}+ E_g +F_{2g} fundamental phonon modes of cubic spinal, respectively. Intense broadband is observed at 700–850 cm^{-1} and is assigned to tetrahedron VO_4 stretching frequencies. This is probably due to the vibration between the highest oxidation state cation (V^{5+}) and oxygen. This broadband is located at 817 cm^{-1} and indicates the A_{1g} symmetry of the VO_4 tetrahedron. While the band in the 327 cm^{-1} region is ascribed to the VO_4 tetrahedron of bending mode with E symmetry. The peak at 372 cm^{-1} indicated Li-O, and the peaks at 505 and 630 cm^{-1} indicated Li-O-Ni asymmetric stretching frequencies [10, 12, 37]. An ideal stretching frequency of VO_4 tetrahedron of Raman spectra is located at 788 cm^{-1}. In lithium nickel vanadate, the observed band was at 788 cm^{-1}, valid for all Li structures. For $LiNiVO_4$, high-frequency band is located at 817 cm^{-1}, which is mainly dependent on Li concentration. Maybe this is because each oxygen is bonded to lithium and nickel cations in the VO_4 tetrahedron [10, 37].

UV–visible studies

Figure 6 indicates the UV–visible spectra of $LiNiVO_4$ NPs. The spectrum clearly shows two absorption bands of 465 and 728 nm. The spectra at longer wavelengths can unmistakably indicate the octahedral d-d spin allowed the transition from Ni^{2+} ion that is $^3A_{2g}$ (F) → $^3T_{1g}$ (F). The band gap shift has two possible charge transfers between respective metal ions [Ni (II), V(V)] and between ligand ions. The one charge transition is from oxygen to central vanadium metal atom (VO_4^{3-}) group. Also, another one is from Ni (II) ion spin allowed d-d transition of $^3A_{2g}$ (F) → $^3T_{1g}$ (P) [7, 33, 34, 39]. Generally, the absorption bands related to metal–ligand and metal–metal charge transfer are difficult to explain because of the presence of expected overlap in the UV–Vis spectral region. The band gap energy of $LiNiVO_4$ NPs was calculated using the Tauc equation from this absorption spectrum [40, 41].

$$\alpha h\upsilon = A(h\upsilon - Eg)^{n/2} \tag{7}$$

Here, α represents the absorption coefficient and hυ related to photon energy, Eg is material band gap, and A is constant. The band gap value of $LiNiVO_4$ NPs was found to

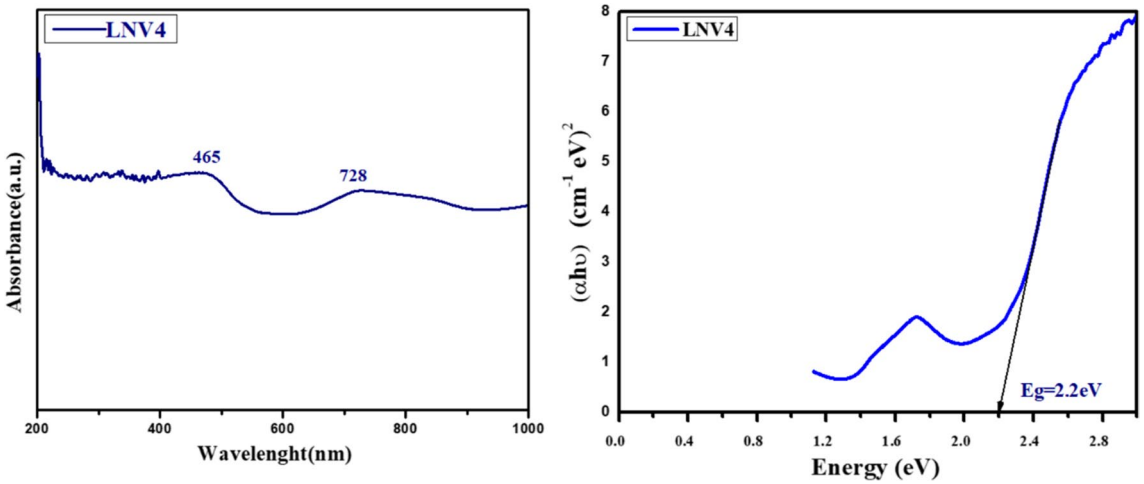

Fig. 6 UV absorbance spectra and Bandgap of lithium nickel vanadate nanoparticles

Table 3 Comparison study of LNV NPs bandgap with other photocatalyst bandgap

Sl no	Samples	Band gap (eV)	References
1	$LiNiVO_4$	2.1	[12]
2	NiV_2O_5	2.29	[23]
3	$Mg_3V_2O_8$	3.02	[42]
4	$Ni_3V_2O_8$	2.25	[42]
5	Zn_3V2O_8	2.92	[42]
6	$FeVO_4$	2.9	[44]
7	$LiNiVO_4$	2.2	Present work

be 2.2 eV [12, 43], which is similar to the reported nickel orthovanadate such as $Ni_3V_2O_8$ (2.25 eV) and NiV_2O_8 (2.29 eV) and is significantly narrower than the alkali earth orthovanadates such as $Mg_3V_2O_8$(3.02 eV), $Zn_3V_2O_8$ (2.92 eV), and $FeVO_4$ (2.9 eV) (Table 3). This indicates that the substitution of Ni^{2+} significantly reduced the band gap of a compound, which is beneficial to the improvement of the photocatalytic activity.

Applications

Photodegradation studies of $LiNiVO_4$ nanoparticles

$LiNiVO_4$ nanoparticles were exposed to visible light for the degradation of MB dye. Some energy absorbed by the nanoparticles is equal to or higher than bandgap energy. It forms the hole (h^+) and electron (e^-) on the surface of the photocatalyst. If the recombination rate of charge carriers is slow, they will start to move to the surface. Then, free electrons undergo reduction and form peroxides/superoxides. Water is oxidized by the hole and forms a hydroxyl radical. Further generated species act as strong oxidizing agents, and these radicals are highly reactive and unstable, finally leading to the degradation of methylene blue dyes/organic dyes. The organic dye is converted into CO_2, H_2O, and some other degradation products, as illustrated in Fig. 7. Photocatalytic activity of nanoparticles on dyes improved by several factors such as crystallinity, phase composition, particle size, structure, size distribution, and band gap. The photocatalytic activity of LNV1, LNV2, LNV3, and LNV4 nanoparticles is represented in Fig. 8. Among these nanoparticles, $LiNiVO_4$ using 8 ml of fuel shows the highest percentage of degradation efficiency on methylene blue dye (Fig. 9). Based on this, we can conclude that $LiNiVO_4$ nanoparticles using 8 ml jack fruit extract as a fuel are used to study the photocatalytic activity for the different parameters [44, 45]. The general mechanism of the photocatalytic activity of $LiNiVO_4$ nanoparticles is proposed as follows.

$$LiNiVO_4 + hv \rightarrow LiNiVO_4\left(e^-_{CB} + h^+_{VB}\right) \tag{8}$$

$$LiNiVO_4 + h^+(hole) \rightarrow \dot{O}H + H^+ \tag{9}$$

$$OH^- + h^+ \rightarrow \dot{O}H(hydroxyl\ radical) \tag{10}$$

$$O_2 + e^- \rightarrow \dot{O}_2^- \tag{11}$$

$$Methylene\ blue + \dot{H}O + \dot{O}_2^- \rightarrow CO_2 + H_2O + degradable\ products \tag{12}$$

The valence and conduction band (E_{VB}, E_{CB}) of the $LiNiVO_4$ nanoparticles were theoretically calculated using the following expression.

$$E_{CB} = \chi\left(A_aB_bC_c\right)^{(1/a+b+c)} - E_0 - 0.5E_g \tag{13}$$

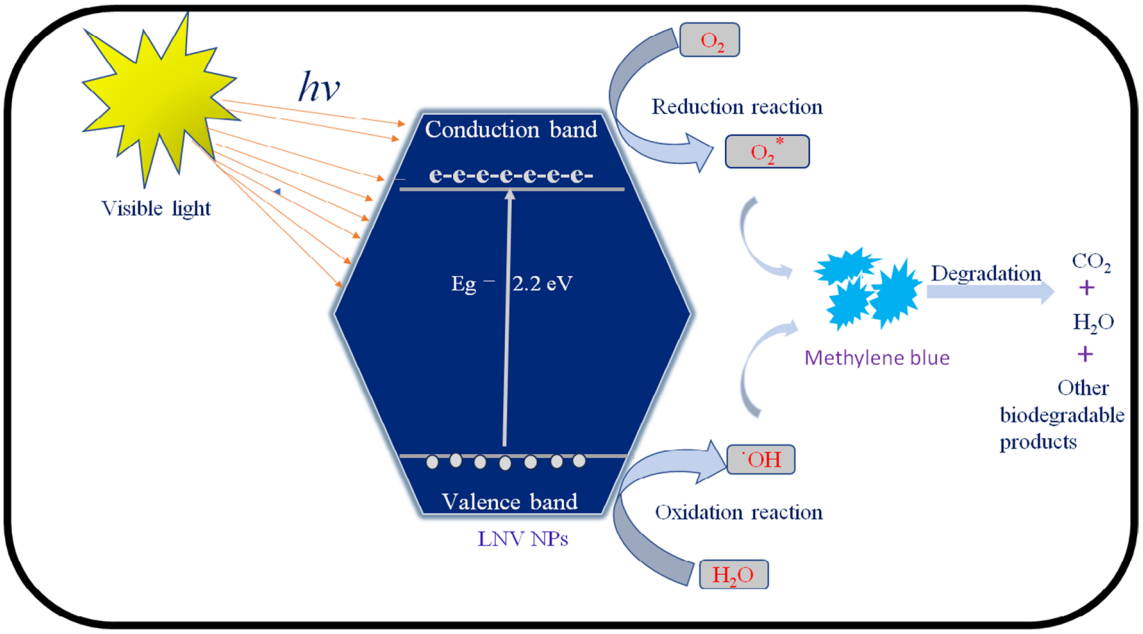

Fig. 7 General photocatalytic degradation mechanism of $LiNiVO_4$ NPs synthesized by combustion method

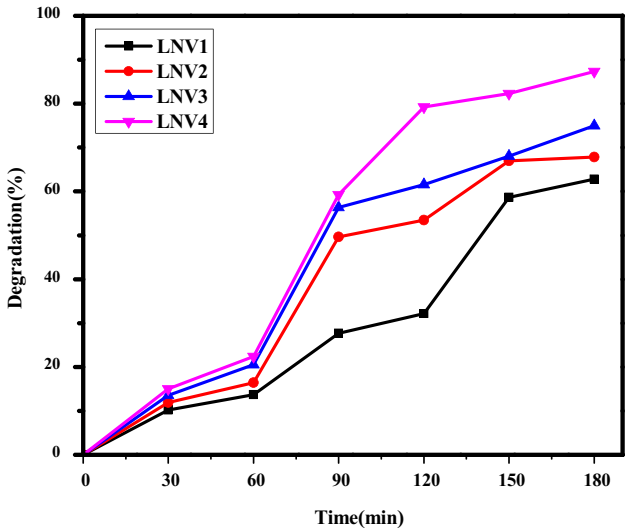

Fig. 8 Photodegradation study of LNV nanoparticles with varied fuel

$$E_{VB} = E_{CB} + E_g \tag{14}$$

Here, χ is the absolute electronegativity, and a, b, and c are the number of atoms in the compound. E_0 is the energy of free electrons on the hydrogen scale (4.5 eV). E_g is the band gap energy of nanoparticles. 5.514 eV is absolute electronegativity, and 2.2 eV is the band gap energy of lithium nickel vanadate nanoparticles. The theoretically calculated valence and conduction band values of $LiNiVO_4$ NPs are 2.11 eV and − 0.036 eV, respectively.

Effect of different concentrations of catalytic load

Different concentrations of photocatalysts (10 to 70 mg) with constant dye concentration (5 ppm) of degradation are represented in Fig. 10. The percentage of degradation varied from 66.15 to 91.77%, and 50 mg of $LiNiVO_4$ shows the highest percentage of degradation. When the catalyst load increases above 50 mg, the degradation percentage starts to decrease due to agglomeration and sedimentation of the catalyst. Also, the size of the particle increases the specific surface area decreases and leads to a decrease in surface active sites. So this concludes that 50 mg of $LiNiVO_4$ nanoparticles shows the highest percentage degradation (91.77%) [45, 46].

Effect of dye concentration

Figure 11 indicates the photodegradation of $LiNiVO_4$ nanoparticles with different concentrations of methylene blue dye. Here, 50 mg of catalyst is taken as constant with a different dye concentration of 5 to 20 ppm at pH-7. The percentage of degradation varies from 91.77 to 64.48% means the lowest concentration of dye (5ppm) shows the highest percentage of degradation [47, 48]. This is because as the dye concentration increases with decreases the penetration of light, it also decreases the active sites on the surface of LNV nanoparticles [32, 49, 50]. This leads to a decrease in degradation [51].

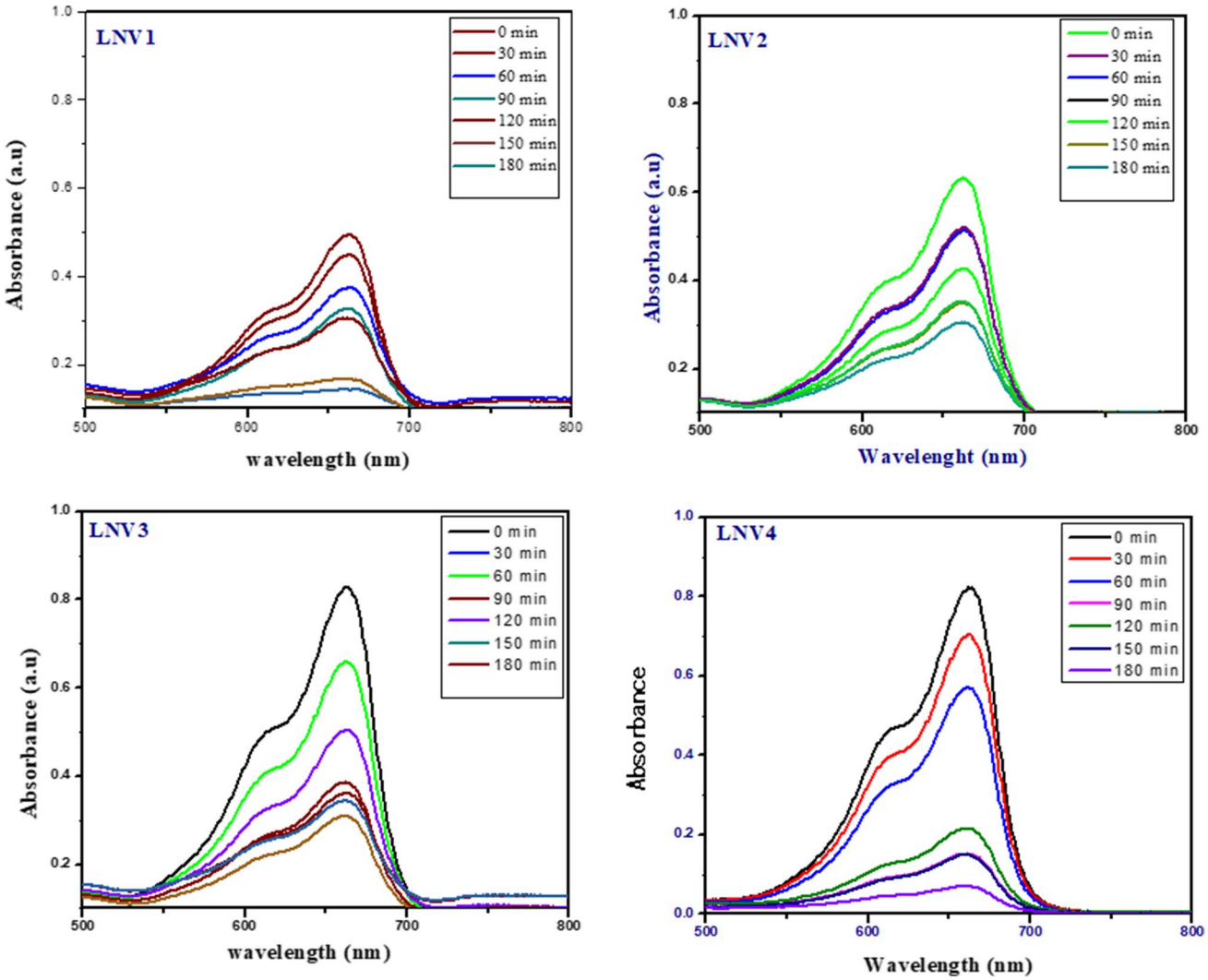

Fig. 9 UV–visible spectra of MB dye during degradation under visible light using LNV (1 to 4) nanoparticles

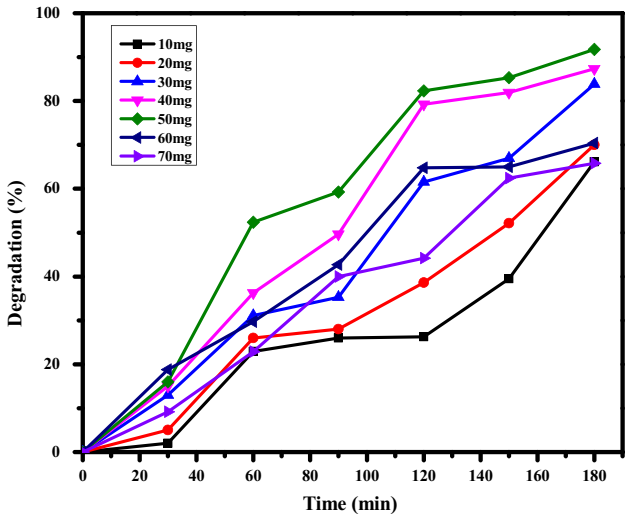

Fig. 10 Degradation of different concentrations of the catalyst under visible radiation

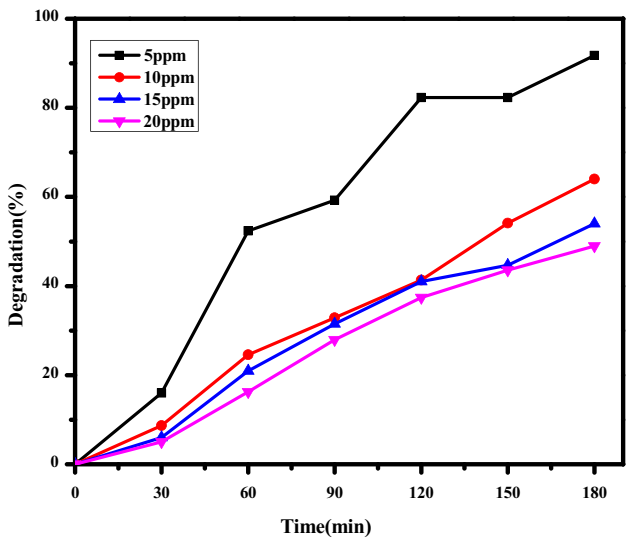

Fig. 11 Variation of MB dye concentration versus irradiation time for LNV catalyst

Effect of different pH on photodegradation

The degradation efficiency of $LiNiVO_4$ nanoparticles on MB dye experiment at different pH was carried out by keeping the concentration of dye and catalyst constant (Fig. 12). It clearly shows that the degradation process mainly depends on the dye solution pH. Using 0.1 M NaOH or 0.1 M HNO_3, the pH of the dye solution was adjusted [52]. The maximum degradation efficiency was observed in the basic medium than in the acidic medium. The pH 10 solution shows the highest percentage of degradation. Above this pH level, the degradation decreases because the surface absorbs negatively charged OH^- ions and leads to a lowering of ˙OH radical production. Strong absorption of dye on the catalyst also decreases the percentage of degradation because it decreases the active sites of the photocatalyst to produce the hydroxyl radicals [55–57]. So the pH solution of 2 to 6 also decreases the percentage of degradation [56].

Scavenger activity on photodegradation

The photocatalytic activity in degradation is mainly due to the photoinduced species, charge separation, and surface redox process. The photocatalytic activity of nanoparticles in organic dye degradation can be increased by identifying the reactive species, which is mainly involved in breaking down the organic dye [57]. To investigate the reactive species which is involved in the photodegradation of methylene blue dye, several scavengers were used. The reactive species are trapped by scavengers and decrease their production. In this study, ethylenediamine tetraacetic acid (EDTA, 1 mM) [57], potassium dichromate ($K_2Cr_2O_7$, 1 mM) [53], and sodium carbonate ($NaCO_3$, 1 mM) [58] are used as a scavenger for h^+ (hole), superoxide (O_2^-), and hydroxyl radicals (˙OH), respectively. Figure 13 reveals that the photodegradation of methylene blue dye without scavengers shows the maximum percentage of degradation. The presence of EDTA and Na_2CO_3 as scavengers decreases the photodegradation of MB dye and indicates that h^+ and hydroxyl radicals are mainly involved in the degradation of MB dye. There is no significant degradation efficiency observed in the presence of the $K_2Cr_2O_7$ scavenger. This reveals O_2^- radical is not significantly involved in the photodegradation of MB dye.

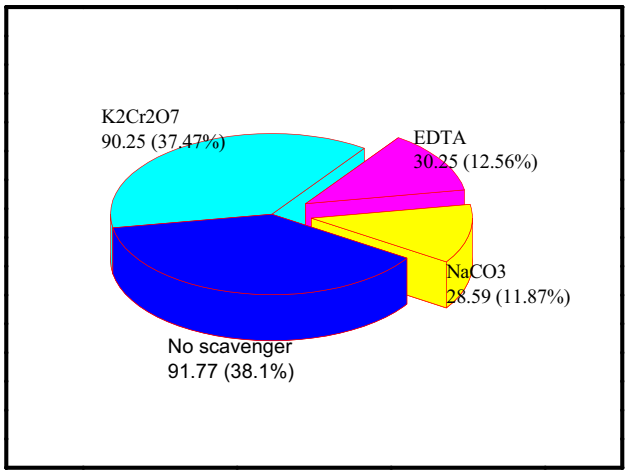

Fig. 13 $LiNiVO_4$ nanoparticles of photocatalytic activity on the MB dye degradation with different scavengers

Recycling of catalyst

To determine the stability of LVN NPs, conduct a recycling experiment of MB dye degradation shown in Fig. 14. This

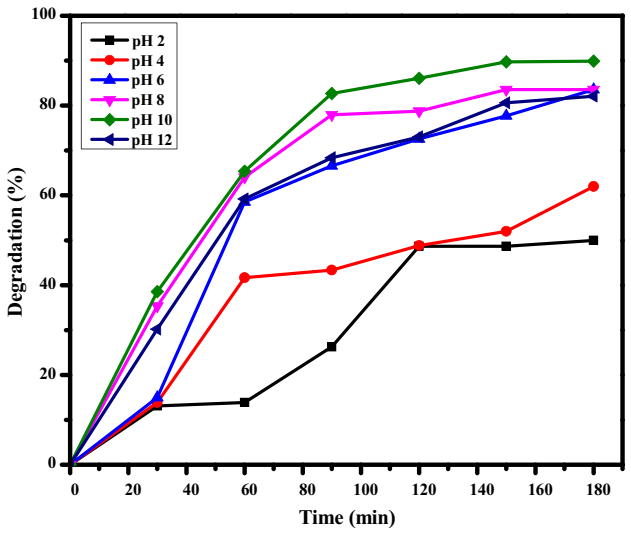

Fig. 12 Percentage degradation of the effect of pH under visible light irradiation

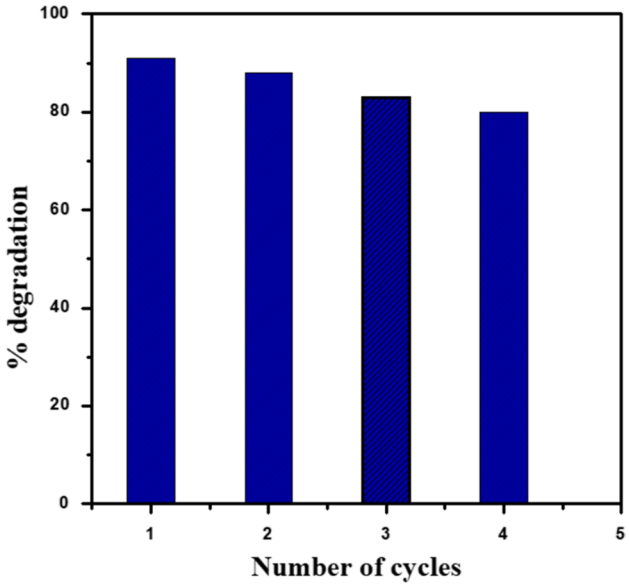

Fig. 14 Recycling study of LVN NPs under visible light

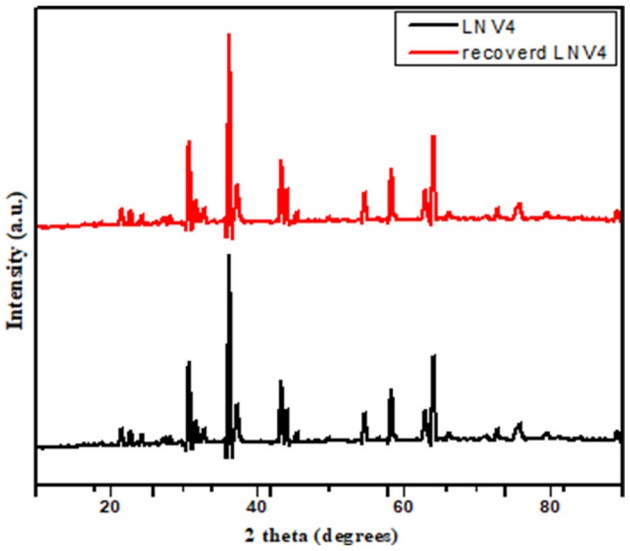

Fig. 15 XRD spectra of recovered LNV4 NPs after completion of fourth cycle of degradation

experiment was carried out using 50 mg LNV catalyst with 100 ml 5 ppm dye. After completing each cycle, the LNV catalyst was washed with distilled water to remove dye residue. Figure 14 indicated that after the completion of 4 cycles, 80% of the dye was degraded by LNV NPs. This concluded the stability of the LNV NPs [59]. The XRD spectra of recovered LNV4 NPs are shown in Fig. 15. This confirmed the stability of LNV4 NPs and showed the same XRD peaks as the initial sample even after the fourth degradation cycle.

Table 4 describes the photodegradation behavior of some typical photocatalyst in the presence of LiNiVO photocatalyst. Among these photocatalysts, $LiNiVO_4$ NPs are synthesized by simple, inexpensive, high yield, and energy-saving combustion method using green extract as fuel. Photocatalytic activity of $LiNiVO_4$ NPs was analyzed using methylene blue dye. It is a common cationic dye and waste product from the textile industries. 91.77% of good degradation efficiency is shown by the LiNiVO4 under visible light illumination at 180 min.

Electrochemical analysis

EIS spectra of synthesized $LiNiVO_4$ NPs are shown in Fig. 16 in the form of a Nyquist plot. The impedance spectroscopy analysis plotted the frequency range between 1 Hz and 1 MHz. In the EIS graph, the semicircle curve represented a high-frequency region, and this corresponds to the charge transfer resistance (Rct) [67]. The next immediate line indicates the low-frequency region and explains the electrochemical reaction that occurs at the electrode controlled by diffusion and charge transfer process. The radius of the semicircle is directly proportional to the charge transfer resistance [68, 69]. Therefore, the smaller the semicircle radius, the higher the charge transfer resistance. The prepared LNVI, LNV2, LNV3, and LNV4 NP capacitance values were found to be 54, 53, 52, and 50, respectively. This data indicated that the LNV4 nanoparticle shows a lower arc radius than the other three nanoparticles. Table 5 shows fitted parameters and conductivity value of LNV NPs. This table explains as R_s value decreases as the conductivity value increases, and at the same time, the C_{dl} value increases as the charge transfer resistance value decreases. This concludes that LNV4 has good ionic conductivity and lower charge transfer resistance [54].

Table 4 Comparison of photodegradation behavior of some typical photocatalysts and the present $LiNiVO_4$ photocatalyst

Materials	Synthesis method	Photodegradation efficiency (%)	Degradation time	Light source used	Organic pollutant (dye)	References
$LiNiVO_4$	Modified Pechini method	95%	240 min	Visible light	Methylene blue	[12]
$CaZnV_2O_7$	Solid state method	95%	240 min	Visible light	Methylene blue	[21]
$NiVO_3$	Hydrothermal method	98.7%	120 min	UV light	Orange red	[22]
Ni_3V2O_8	Hydrothermal	57.66%	90 min	UV light	Methylene blue	[23]
Ni_2FeVO_6	Sol–gel method	88%	120 min	Visible light	Methylene blue	[24]
V_2O_5	Hydrothermal method	84%	90 min	UV light	Methyl orange	[60]
V_2O_5	Physicochemical reduction method	92%	60 min	visible light	Methylene blue	[61]
V_2O_5	Hydrothermal	85%	300 min	Visible light	Rhodamine 6G	[62]
V_2O_5	Flame spray pyrolysis	81%	120 min	Visible light	Methylene blue	[63]
V_2O_5	Hydrothermal	28.14%	180 min	Visible light	Congo red	[64]
V_2O_5	Hydrothermal method	68%	80 min	Visible light	Methylene blue	[65]
V_2O_5	Hydrothermal method	80%	180 min	Sun light	Methylene blue	[66]
$LiNiVO_4$	Combustion method	91.77%	180 min	Visible light	Methylene blue	Present work

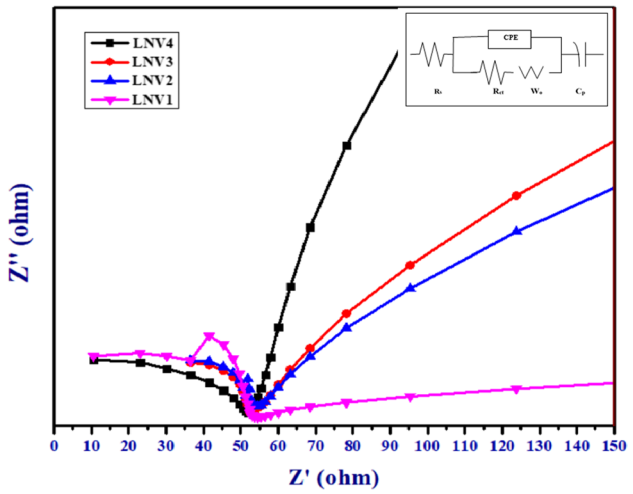

Fig. 16 Electrochemical impedance spectroscopy plot of different LNV nanoparticles

Table 5 Summarized table for EIS fitted parameters of LNV NPs

Material	R_s (kΩ)	C_{dl} (nF)	R_{ct} (Ω cm^2)	Conductivity S cm^{-1} (1/R)
LNV 1	10.86	1.14×10^{-4}	52.95	2.4×10^{-2}
LNV 2	36.12	1.15×10^{-4}	54.58	2.1×10^{-2}
LNV 3	36.12	1.25×10^{-4}	52.43	2.0×10^{-2}
LNV 4	10.86	1.29×10^{-4}	51.05	2.6×10^{-2}

Figure 17 shows the angular frequency dependence of Z' and Z'' of LNV4 NPs. Figure 17a shows the variation of the impedance's real part (Z′) as a function of frequency. The decrease in Z′ magnitude at lower frequencies indicates the grain resistance reduction. Figure 17b shows the variation of Z″ with frequency.

Conclusion

This work provided a successfully synthesized lithium nickel vanadate photocatalyst by simple combustion method using jackfruit seed extract as fuel. The average crystalline size of the nanoparticle is 55 nm. Due to the narrow band gap (2.2 eV) of LNV NPs, exhibit its photocatalytic activity in the degradation of organic dye under visible light illumination. Hence, the inverse spinal structure of 50 mg of LNV4 NPs demonstrated efficient degradation under visible light irradiation for 180 min, achieving a degradation efficiency of 91.77%. The post-photocatalytic XRD analysis confirmed the chemical stability of the LNV NPs. Electrochemical impedance spectroscopy analysis revealed that LNV NPs were suitable for the supercapacitor preparation. The lower charge transfer and good ionic conductivity were shown by EIS analysis. This study successfully demonstrates that the simple and environmentally friendly synthesis of $LiNiVO_4$ NPs using aqueous jackfruit seed extract and their promising characteristics make them a potential candidate for various environmentally and health-related applications such as photodegradation and electrochemical.

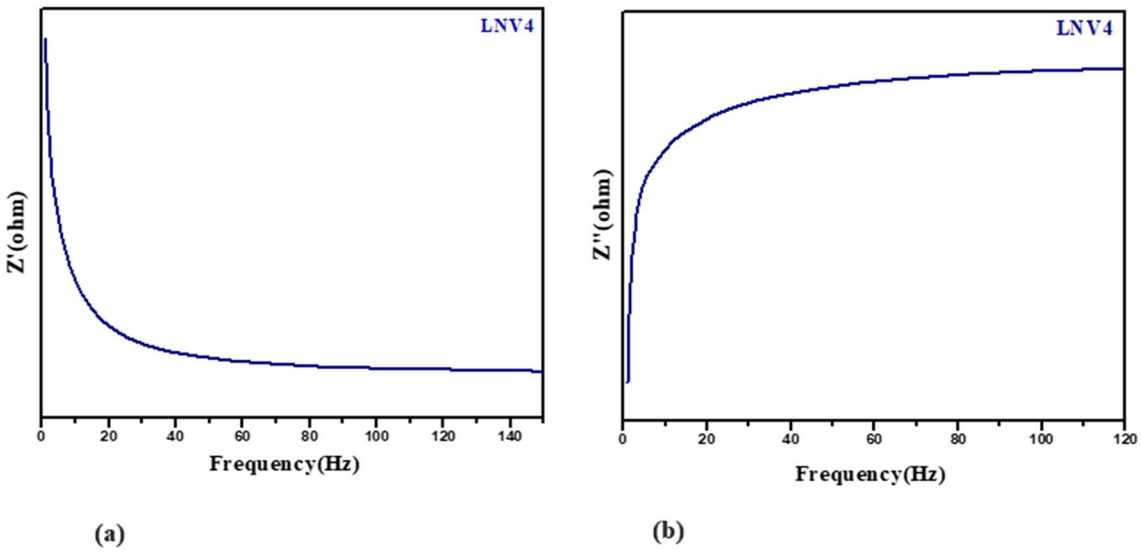

Fig. 17 Frequency vs. Z′ (**a**) and Z″ (**b**) graph of LNV NPs

Acknowledgements Authors acknowledge JSS College of Arts, Commerce and Science, Ooty Road, Mysuru, The National Institute of Engineering, Manandavadi Road, Mysuru, and also Siddaganaga Institute of Technology, Tumkuru for laboratory facility.

Author contribution Thejaswini M: Data acquisition, writing – original draft, Nagaraju G, Lakshmi Ranganatha V, Mallikarjunaswamy C, Pramila S: review.

Data Availability No datasets were generated or analysed during the current study.

Declarations

Consent for publication Not applicable.

Competing interests The authors declare no competing interests.

References

1. Feynman RP (1992) There's plenty of room at the bottom. I(I):60–66
2. El-Rafie HM, El-Rafie MH, Zahran MK (2013) Green synthesis of silver nanoparticles using polysaccharides extracted from marine macro algae. Carbohydr Polym 96(2):403–410. https://doi.org/10.1016/j.carbpol.2013.03.071
3. Ghiyasiyan-Arani M, Salavati-Niasari M (2020) Strategic design and electrochemical behaviors of Li-ion battery cathode nanocomposite materials based on AlV_3O_9 with carbon nanostructures. Compos Part B Eng 183:107734. https://doi.org/10.1016/j.compositesb.2019.107734
4. Prakash D, Masuda Y, Sanjeeviraja C (2013) Synthesis and structure refinement studies of $LiNiVO_4$ electrode material for lithium rechargeable batteries. Ionics (Kiel) 19(1):17–23. https://doi.org/10.1007/s11581-012-0720-1
5. Hua K et al (2019) Cation-exchange synthesis of manganese vanadate nanosheets and its application in lithium-ion battery. J Solid State Chem 273:287–294. https://doi.org/10.1016/j.jssc.2019.02.026
6. Prakash D, Masuda Y, Sanjeeviraja C (2013) Structural, electrical and electrochemical studies of $LiCoVO_4$ cathode material for lithium rechargeable batteries. Powder Technol 235:454–459. https://doi.org/10.1016/j.powtec.2012.10.042
7. Myung ST, Amine K, Sun YK (2015) Nanostructured cathode materials for rechargeable lithium batteries. J Power Sources 283:219–236. https://doi.org/10.1016/j.jpowsour.2015.02.119
8. Ismail L, Ramesh S, Winie T, Arof AK (2011) Mixed doped lithium nickel vanadate as cathode material by sol-gel and polymer precursor method. Mater Res Innov 15(SUPPL.) 2. https://doi.org/10.1179/143307511X13031890748056
9. Zhao Z et al (2005) A low-temperature molten salt synthesis of $LiNiVO_4$ cathode material for lithium ion batteries. J Am Ceram Soc 88(9):2622–2624. https://doi.org/10.1111/j.1551-2916.2005.00462.x
10. Bhuvaneswari MS, Selvasekarapandian S, Kamishima O, Kawamura J, Hattori T (2005) Vibrational analysis of lithium nickel vanadate. J Power Sources 139(1–2):279–283. https://doi.org/10.1016/j.jpowsour.2004.07.006
11. Sakunthala A Synthesis and characterization of ltihium. (M):450–455
12. Qiao X, Huang Y, Seo HJ (2014) Optical property and visible-light-driven photocatalytic activity of inverse spinel $LiNiVO_4$ nanoparticles prepared by Pechini method. Appl Surf Sci 321:488–494. https://doi.org/10.1016/j.apsusc.2014.10.029
13. Zhang S, Zhong Q, Wang Y (2014) Effect of rutile phase on V_2O_5 supported over TiO_2 mixed phase for the selective catalytic reduction of NO with NH_3. Appl Surf Sci 314:112–118. https://doi.org/10.1016/j.apsusc.2014.06.118
14. Song L, Liu S, Lu Q, Zhao G (2012) Fabrication and characterization of electrospun orthorhombic $InVO_4$ nanofibers. Appl Surf Sci 258(8):3789–3794. https://doi.org/10.1016/j.apsusc.2011.12.029
15. Oshikiri M, Boero M, Matsushita A, Ye J (2008) Dissociation of water molecule at three-fold oxygen coordinated V site on the $InVO_4$ (0 0 1) surface. Appl Surf Sci 255(3):679–681. https://doi.org/10.1016/j.apsusc.2008.07.041
16. Sottmann J et al (2022) 5D total scattering computed tomography reveals the full reaction mechanism of a bismuth vanadate lithium ion battery anode. Phys Chem Chem Phys 11(1):27075–27085. https://doi.org/10.1039/d2cp03892g
17. Zhou C et al (2013) Bubble template synthesis of $Sn_2Nb_2O_7$ hollow spheres for enhanced visible-light-driven photocatalytic hydrogen production. Chem Commun 49(84):9872–9874. https://doi.org/10.1039/c3cc45683h
18. Vu TA et al (2014) Synthesis of novel silver vanadates with high photocatalytic and antibacterial activities. Mater Lett 123:176–180. https://doi.org/10.1016/j.matlet.2014.03.004
19. Paquin F, Rivnay J, Salleo A, Stingelin N, Silva C (2015) Multi-phase semicrystalline microstructures drive exciton dissociation in neat plastic semiconductors. J Mater Chem C 3(207890):10715–10722. https://doi.org/10.1039/b000000x
20. Liu Q, Yang J, Sun X, Cheng X, Tang H, Li H (2014) Influence of W doped ZrV_2O_7 on structure, negative thermal expansion property and photocatalytic performance. Appl Surf Sci 313:41–47. https://doi.org/10.1016/j.apsusc.2014.05.120
21. Wang J, Qin L, Huang Y, Cai P, Jin Seo H (2014) Preparation and photocatalytic activities of pyrovanadate $CaZnV_2O_7$ under visible light irradiation. Mater Lett 125:89–91. https://doi.org/10.1016/j.matlet.2014.03.065
22. Naik LR et al. (2023) Hydrothermal synthesis and characterization of nanostructured nickel vanadate for supercapacitor and photocatalytic applications. Mater Res Express 10(12). https://doi.org/10.1088/2053-1591/ad184c
23. Naik Ramavathu L, Rao Harapanahalli S, Pernapati N, Tumma B (2021) Synthesis and characterization of nickel metavanadate ($Ni_3V_2O_8$)-application as photocatalyst and supercapacitor. Int J Nano Dimens 12(4):411–421. https://doi.org/10.22034/IJND.2021.682472
24. Qiao X, Huang Y, Cheng H, Seo HJ (2015) Surface properties, simultaneous photocatalytic and magnetic activities of Ni_2FeVO_6 nanoparticles. Appl Surf Sci 359:259–265. https://doi.org/10.1016/j.apsusc.2015.10.112
25. Vesali-Kermani E, Habibi-Yangjeh A, Ghosh S (2020) Efficiently enhanced nitrogen fixation performance of g-C_3N_4 nanosheets by decorating $Ni_3V_2O_8$ nanoparticles under visible-light irradiation. Ceram Int 46(15):24472–24482. https://doi.org/10.1016/j.ceramint.2020.06.232
26. Kannan SK, Hareendrakrishnakumar H, Joseph MG (2021) Efficient polysulfide shuttle mitigation by graphene-lithium cobalt vanadate hybrid for advanced lithium-sulfur batteries. J Electroanal Chem 899(June):115665. https://doi.org/10.1016/j.jelechem.2021.115665
27. Sangeetha G, Rajeshwari S, Venckatesh R (2011) Green synthesis of zinc oxide nanoparticles by aloe barbadensis miller leaf extract: structure and optical properties. Mater Res Bull 46(12):2560–2566. https://doi.org/10.1016/j.materresbull.2011.07.046
28. Rathnasamy R, Thangasamy P, Thangamuthu R, Sampath S, Alagan V (2017) Green synthesis of ZnO nanoparticles using Carica

papaya leaf extracts for photocatalytic and photovoltaic applications. J Mater Sci Mater Electron 28(14):10374–10381. https://doi.org/10.1007/s10854-017-6807-8
29. Zheng Y et al (2015) Green biosynthesis and characterization of zinc oxide nanoparticles using Corymbia citriodora leaf extract and their photocatalytic activity. Green Chem Lett Rev 8(2):59–63. https://doi.org/10.1080/17518253.2015.1075069
30. Siripireddy B, Mandal BK (2017) Facile green synthesis of zinc oxide nanoparticles by Eucalyptus globulus and their photocatalytic and antioxidant activity. Adv Powder Technol 28(3):785–797. https://doi.org/10.1016/j.apt.2016.11.026
31. Soto-Robles CA et al (2018) Biosynthesized zinc oxide using Lycopersicon esculentum peel extract for methylene blue degradation. J Mater Sci Mater Electron 29(5):3722–3729. https://doi.org/10.1007/s10854-017-8305-4
32. Mallikarjunaswamy C, Pramila S, Nagaraju G, Ramu R, Ranganatha VL (2021) Green synthesis and evaluation of antiangiogenic, photocatalytic, and electrochemical activities of $BiVO_4$ nanoparticles. J Mater Sci Mater Electron 32(10):14028–14046. https://doi.org/10.1007/s10854-021-05980-w
33. Reddy MV, Pecquenard B, Vinatier P, Levasseur A (2006) Effect of substrate temperature on morphology and electrochemical performance of radio frequency magnetron sputtered lithium nickel vanadate films used as negative electrodes for lithium microbatteries. J Phys Chem B 110(9):4301–4306. https://doi.org/10.1021/jp0565554
34. Bhuvaneswari MS, Selvasekarapandian S, Kamishima O, Kawamura J, Hattori T (2005) Synthesis and structural analysis of lithium nickel vanadate. Mater Chem Phys 91(1):94–98. https://doi.org/10.1016/j.matchemphys.2004.10.054
35. Lee SJ, Lee HY, Ha TS, Baik HK, Lee SM (2002) Amorphous lithium nickel vanadate thin-film anodes for rechargeable lithium microbatteries. Electrochem Solid-State Lett 5(6):139–141. https://doi.org/10.1149/1.1477298
36. Vivekanandhan S, Venkateswarlu M, Satyanarayana N (2004) Glycerol-assisted gel combustion synthesis of nano-crystalline $LiNiVO_4$ powders for secondary lithium batteries. 58:1218–1222. https://doi.org/10.1016/j.matlet.2003.09.011
37. Liu J, Wang M, Lin X, Yin D, Huang W (2002) Citric acid complex method of preparing inverse spinel $LiNiVO_4$ cathode material for lithium batteries 108:113–116
38. Fey GT, Perng W (1997) Materials Science Communication A new preparation method for a novel high voltage cathode material 47:279–282
39. Hareendrakrishnakumar H, Chulliyote R, Joseph MG (2018) Effect of crystallite size on the intercalation pseudocapacitance of lithium nickel vanadate in aqueous electrolyte. J Solid State Electrochem 22(1):1–9. https://doi.org/10.1007/s10008-017-3712-2
40. Julien C, Massot M, Pe C (2018) Cathodes materials for Li-ion batteries. 4(May 2000): 0–7. https://doi.org/10.1016/S0921-5107(99)00601-7
41. Prabaharan SRS, Michael MS, Radhakrishna S, Julien C, Curie M (1997) Novel low-temperature synthesis and characterization of LiNiVO for high-voltage Li ion batteries. 7(9):1791–1796
42. Mg VPMVOM, Wang D, Tang J, Zou Z, Ye J (2005) Photophysical and photocatalytic properties of a new series of. 8(2):5177–5182
43. Biswas SK, Dhak D, Pathak A, Pramanik P (2008) Chemical synthesis of environment-friendly nanosized yellow titanate pigments. Mater Res Bull 43(3):665–675. https://doi.org/10.1016/j.materresbull.2007.04.001
44. Ghiyasiyan-Arani M, Salavati-Niasari M, Naseh S (2017) Enhanced photodegradation of dye in waste water using iron vanadate nanocomposite; ultrasound-assisted preparation and characterization. Ultrason Sonochem 39:494–503. https://doi.org/10.1016/j.ultsonch.2017.05.025
45. Mallikarjunaswamy C, Parameswara P, Pramila S, Nagaraju G, Deepakumari HN, Lakshmi Ranganatha V (2022) Green and facile synthesis of zinc oxide nanoparticles for enhanced photocatalytic organic pollutant degradation. J Mater Sci Mater Electron 33(25):20361–20372. https://doi.org/10.1007/s10854-022-08852-z
46. Mallikarjunaswamy C, Lakshmi Ranganatha V, Ramu R, Udayabhanu, Nagaraju G (2020) Facile microwave-assisted green synthesis of ZnO nanoparticles: application to photodegradation, antibacterial and antioxidant. J Mater Sci Mater Electron 31(2):1004–1021. https://doi.org/10.1007/s10854-019-02612-2
47. Pramila S, Ranganatha VL, Soundarya TL, Ramu R, Nagaraju G, Mallikarjunaswamy C (2022) Eco-mediated synthesis of visible active Bi_2WO_6 nanoparticles and its performance towards photocatalyst, supercapacitor, biosensor, and antioxidant activity. J Clust Sci 33(5):2233–2248. https://doi.org/10.1007/s10876-021-02147-9
48. Mallikarjunaswamy C et al. (2023) Facile synthesis of multifunctional bismuth oxychloride nanoparticles for photocatalysis and antimicrobial test. Mater Sci Eng B Solid-State Mater Adv Technol 290(February):116323. https://doi.org/10.1016/j.mseb.2023.116323
49. Martin F-D, Müller-Buschbaum H (1994) Zur Kenntnis von $KBa_2V_2O_7Cl$ / On KBa_2 V_2O_7 Cl. Zeitschrift für Naturforschung B 49(8):1141–1144. https://doi.org/10.1515/znb-1994-0820
50. Mallikarjunaswamy PS, Ranganatha CL (2024) $BiVO_4$ nanoballs : a simple precipitation pathway , promising electrochemical sensor , and photodegradation under visible light. no. 0123456789. https://doi.org/10.1007/s11581-024-05460-1
51. M. Swamy M, S. BS, M. C, P. S, and ND R. (2021) Bio-mediated synthesis of ZnO nanoparticles using Lantana Camara flower extract: its characterizations, photocatalytic, electrochemical and anti-inflammatory applications. Environ Nanotechnology Monit Manag 15(February):100442. https://doi.org/10.1016/j.enmm.2021.100442
52. Pavithra NS, Lingaraju K, Raghu GK, Nagaraju G (2017) Citrus maxima (Pomelo) juice mediated eco-friendly synthesis of ZnO nanoparticles: applications to photocatalytic, electrochemical sensor and antibacterial activities. Spectrochim Acta - Part A Mol Biomol Spectrosc 185:11–19. https://doi.org/10.1016/j.saa.2017.05.032.
53. Pramila S, Ranganatha VL, Nagaraju G, Mallikarjunaswamy C (2022) Green synthesis of bismuth tungstate nanoparticles, evaluation of their applications favouring photocatalytic and bio-sensing. Inorg Nano-Metal Chem 0(0):1–13. https://doi.org/10.1080/24701556.2022.2081192
54. Lakshmi Ranganatha V, Pramila S, Nagaraju G, Udayabhanu, Surendra BS, Mallikarjunaswamy C (2020) Cost-effective and green approach for the synthesis of zinc ferrite nanoparticles using Aegle Marmelos extract as a fuel: catalytic, electrochemical, and microbial applications. J Mater Sci Mater Electron 31(20):17386–17403. https://doi.org/10.1007/s10854-020-04295-6
55. Pramila S et al. (2020) Green synthesis of $BiVO_4$ nanoparticles by microwave method using Aegle marmelos juice as a fuel : photocatalytic and antimicrobial study. https://doi.org/10.1080/22297928.2020.1785935
56. Udayabhanu et al (2017) Vitis labruska skin extract assisted green synthesis of ZnO super structures for multifunctional applications. Ceram Int 43(15):11656–11667. https://doi.org/10.1016/j.ceramint.2017.05.351
57. Basavalingaiah KR, Udayabhanu, Harishkumar S, Nagaraju G, Chikkahanumantharayappa (2020) Uniform deposition of silver dots on sheet like $BiVO_4$ nanomaterials for efficient visible light active photocatalyst towards methylene blue degradation. FlatChem 19:100142 https://doi.org/10.1016/j.flatc.2019.100142

58. Omrani N, Nezamzadeh-Ejhieh A (2020) Focus on scavengers' effects and GC-MASS analysis of photodegradation intermediates of sulfasalazine by Cu_2O/CdS nanocomposite. Sep Purif Technol 235:116228. https://doi.org/10.1016/j.seppur.2019.116228
59. Sarathi R, Sheeba NL, Selva Essaki E, Sundar SM (2022) Titanium doped zinc oxide nanoparticles: a study of structural and optical properties for photocatalytic applications. Mater Today Proc 64(xxxx):1859–1863. https://doi.org/10.1016/j.matpr.2022.06.387
60. Raj AT, Ramanujan K, Thangavel S, Gopalakrishan S (2015) Facile synthesis of vanadium-pentoxide nanoparticles and study on their electrochemical. no. December 2014. https://doi.org/10.1166/jnn.2015.9543
61. Badreldin A et al (2021) Surface microenvironment engineering of black V_2O_5 nanostructures for visible light photodegradation of methylene blue. J Alloys Compd 871:159615. https://doi.org/10.1016/j.jallcom.2021.159615
62. Kumar S, Sadishkumar V, Arun T (2018) Materials Science in Semiconductor Processing Enhanced photocatalytic activity of V_2O_5 nanorods for the photodegradation of organic dyes : a detailed understanding of the mechanism and their antibacterial activity. Mater Sci Semicond Process 85(June):122–133. https://doi.org/10.1016/j.mssp.2018.06.006
63. Kruefu V, Sintuya H, Pookmanee P, Phanichphant S (2017) Visible light photocatalytic degradation of methylene blue using V_2O_5 nanoparticles. (V):62–67
64. Sajid MM et al. (2020) Preparation and characterization of vanadium pentoxide (V_2O_5) for. Surfaces and Interfaces 100502. https://doi.org/10.1016/j.surfin.2020.100502
65. Babar BM et al (2022) Hydrothermally prepared vanadium oxide nanostructures for photocatalytic application. ES Energy Environ 15:82–91. https://doi.org/10.30919/esee8c639
66. Le TK, Kang M, Kim SW (2019) Morphology engineering, room-temperature photoluminescence behavior, and sunlight photocatalytic activity of V_2O_5 nanostructures. Mater Charact 153(December 2018):52–59. https://doi.org/10.1016/j.matchar.2019.04.046
67. Vasudha M et al. (2021) Facile chemical synthesis of $Ca_3MgAl_{10}O_{17}$ nanomaterials for photocatalytic and non-enzymatic sensor applications. Sensors Int 2(December 2020):100082. https://doi.org/10.1016/j.sintl.2021.100082
68. Surendra BS, Swamy MM, Shamala T, Rao S, Pramila S. Sensors International, no. xxxx
69. Cachet (2009) Άλλες Ουσίες Από Τις Οποίες Ουσίες Που Ντοπάρισμα Των Ζώων Πρόληψη - Θεραπεία Μονοξείδιο Του Άνθρακα (Co) Συνθήκες Που Ευνοούν Την Εμφάνιση Δηλητηριάσεων Από Co Μηχανισμός Τοξικότητας Του Co Μηχανισμός Τοξικότητας Του Co. Gynecol Oncol 141(2016):21–22. https://doi.org/10.1016/j.ygyno.2016.04.081